IEEE Access
Multidisciplinary | Rapid Review | Open Access Journal

Received November 28, 2018, accepted December 11, 2018, date of publication January 9, 2019, date of current version March 20, 2019.

Digital Object Identifier 10.1109/ACCESS.2019.2891058

Compact Broadband Triple-Ring Five-Port Reflectometer for Microwave Brain Imaging Applications

TOUFIQ MD HOSSAIN[1], MOHD FAIZAL JAMLOS[1], (Senior Member, IEEE), MOHD AMINUDIN JAMLOS[2,3], PING JACK SOH[2], (Senior Member, IEEE), SITI ZURAIDAH IBRAHIM[2], MUAMMAR MOHAMAD ISA[4], DOMINIQUE M. M.-P. SCHREURS[5], (Fellow, IEEE), ADAM NARBUDOWICZ[6], (Member, IEEE), AND MOHD FAIRUSHAM GHAZALI[1,7]

[1]Faculty of Mechanical Engineering, Universiti Malaysia Pahang, Pekan 26600, Malaysia
[2]Advanced Communication Engineering Centre, School of Computer and Communication Engineering, Universiti Malaysia Perlis, Kangar 01000, Malaysia
[3]Department of Electronics Engineering, Faculty of Technology Engineering, Universiti Malaysia Perlis, Kangar 01000, Malaysia
[4]School of Microelectronic Engineering, Universiti Malaysia Perlis, Kangar 01000, Malaysia
[5]Division ESAT-TELEMIC, Department of Electrical Engineering, KU Leuven, 3000 Leuven, Belgium
[6]Antenna and High Frequency Research Centre, School of Electrical and Electronic Engineering, Dublin Institute of Technology, Dublin 02, D08 X622, Ireland
[7]Centre of Excellence for Advanced Research in Fluid Flow, Universiti Malaysia Pahang, Pekan 26300, Malaysia

Corresponding author: Mohd Faizal Jamlos (mohdfaizaljamlos@gmail.com)

This work was supported in part by the CREST Fund under Grant P12C2-17, Grant FRGS/1/2017/TK03/UMP/02/1, Grant PRGS/1/2018/ICT06/UNIMAP/02/5, and Grant MOHE FRGS/1/2017/STG02/UNIMAP/02/2, in part by the Marie Skłodowska-Curie under Grant 713567, and in part by the Science Foundation Ireland (SFI) under Grant 13/RC/2077.

ABSTRACT The broadband five-port reflectometer (FPR) is proposed using a triple-ring based technique. The design introduces a tapering in the inter-ring transmission lines (TLs), which provides additional degrees of freedom for optimization and contributes to increased bandwidth. The miniaturization strategy allows incorporating the third ring without significant size increase. In addition, a method for expressing the effective physical dimension of a planar symmetric FPR is also presented in an easily comprehensible way, which can be implemented for other symmetric planar junctions with more than four ports. The proposed design comprises three concentric rings with phase-shifting arrangements between the inter-ring TLs and outer matching arm sections. Inter-ring TLs are shifted by 36° (half factorized value of the inter-port angular distance of 72°) in three different optimizing steps. Tapered TLs have been used between two consecutive rings to achieve very wide bandwidth of at least 88% in simulations and at least 85% in measurements. Curved matching TLs are used in the final design, yielding a compact size of $0.397\lambda_g \times 0.377\lambda_g$ with 43% reduction in length and 43% in width compared to its non-compact counterpart. Genetic algorithm and quasi-Newton algorithm are used in optimizing the final prototype for operation in the frequency band used for brain microwave imaging. The proposed FPR realized a fractional bandwidth of at least 85% (from 0.96 to 2.38 GHz) with a reflection coefficient below -20 dB and a -6 ± 1 dB transmission coefficient with the required phase shift of $\pm 120°$ between different ports. The measured results agree well with the simulation. Finally, the overall imaging system setup and image construction algorithm are presented and discussed for possible incorporation with this FPR for brain microwave imaging.

INDEX TERMS Five-port reflectometer, microwave imaging.

I. INTRODUCTION

Brain injury is a serious medical emergency. Each year, 15 million people suffer from brain stroke attack, among which 5 million result in fatality [1]. A similar number of victims are subjected to post-attack permanent disabilities, as three-quarter of the overall affected patients are inaccessible to affordable brain imaging [1], [2]. To perform accurate medical treatment, it is imperative to determine the type of stroke. A portable low-cost brain imaging

The associate editor coordinating the review of this manuscript and approving it for publication was Yingsong Li.

system is therefore a much needed device, especially if it can be used within short-time after the attack (normally within 4.5 hours) [3]. This system can be carried by the paramedic team in the ambulance or can easily be set up in rural clinics to ensure early diagnosis of brain in the event of a stroke.

Microwave imaging using Vector Network Analyzer (VNA) [4], [5], has attracted the interest of researchers as an excellent non-invasive and cost-effective complementary approach to the contemporary diagnostic tools for brain imaging [6]. The goal of achieving higher penetration depth without compromising the image resolution is fulfilled by choosing the frequency range of 1 to 4 GHz [18]–[20]. However, VNAs are expensive and fragile, and therefore not suitable as a portable imaging solution [13], [18]. In place of this, a low-cost and portable solution is the multiport reflectometer [21], [22]. A multiport reflectometer is a passive network where two of the ports are dedicated for input power source and Device-Under-Test (DUT), respectively, whereas at least three ports (in case of five-port reflectometer) are connected to scalar power detectors. The ratio between each of the detected power, P_k (where k is the number of port to which the detector is attached) to the reference power, P_{ref}, scribes a circle in the complex reflection coefficient (Γ) plane [23]. The intersection point of these circles determines the DUT's complex scattering parameters. Different Six Port Reflectometers (SPRs) have been presented by researchers in [7]–[9], [21], [22], [24], and [25]. Among these, [21] and [22] are designed for microwave imaging applications. Double-ring-based designs with and without tapered matching TLs are presented in [11] and [26], respectively. However, a SPR needs more power detectors compared to a five–port solution, leading to additional cost of the system, especially for multistatic radar imaging systems. Moreover, SPR requires additional microwave components [14], and the matching properties affect the appropriate detection of the scattering characteristics of the DUT [27]. This, in turn, will affect the imaging system. In comparison to SPR [7], [8], a Five-Port Reflectometer (FPR) facilitates the attainment of a 120° relative phase distribution between complex quantities q_k, based on Engen [28]. Moreover, FPR does not require reference power detector, enabling faster and cost effective measurements [29]. Comparison between SPRs (in the range of 1 to 4 GHz) and different FPRs is presented in Table 1 in terms of fractional bandwidth and size. A threshold value of -20 dB in terms of reflection coefficient defines the bandwidth of the FPR [15], [17], and is used as a common benchmark in the comparison between literatures. On the other hand, sizes of the reflectometers are calculated in terms of wavelength based on the lowest operating frequency.

Table 1 shows the highest fractional bandwidth achieved in recent literature is 54.54 % for SPR, within the range of 1 to 4 GHz, a band generally used for brain microwave imaging. Single ring junction FPR (otherwise known as fundamental symmetric FPR) is capable of achieving a fractional bandwidth of 10 % [17]. The fractional bandwidth of single ring junction in [14] is enhanced to 26 % when integrating a superstrate. However, this is at the expense of fabrication complexity. Furthermore, matching circuits can be used in each of the five arms of the single ring design to boost fractional bandwidth to 52.86 % as in [13]. Next, a double ring-based design was presented with non-shifted design and non-tapered matching TL in [17], whereas a shifted design with tapered matching TL were studied in [16]. The fractional bandwidths in [16] and [17] are 76 % and 64 %, respectively. These investigations indicated the possibility of enhancing the bandwidth of FPR using a higher number of rings (more than two), with the inclusion of tapered TL for further matching purposes. Moreover, size miniaturization can be achieved using curved lines as presented in [30]. However, as the work in [30] is not focused on enhancing the fractional bandwidth, the single ring topology used featured only 10 % of bandwidth.

TABLE 1. Comparison of different multiport reflectometers*.

Ref.	No. of ports	Operating band (GHz)	$BW_{-20\,dB}$ (%)	Size
[7]	6	2-3.5	54.54%	Not given
[8]	6	1.6-2.2	32%	0.676 λ×0.103 λ
[9]	6	2.5-3.5	33.33%	0.467 λ×0.408 λ
[10]	6	2.5-4	46.15%	2λ × 0.667λ
[11]	6	2.1-2.75	26.80%	0.38λ×0.33λ
[12]	6	1.04-1.62	44%	0.306 λ×0.266 λ
[13]	5	1.6-2.75	52.86%	0.26 λ×0.25λ
[14]	5	2.34–3.04	26%	0.156λ×0.148λ
[15]	5	0.68-0.74	12%	(0.417λ×0.397λ)*
[16]	5	1.57-3.5	76%	(0.38λ×0.36λ)*
[17]	5	5-9.71	64%	(0.796λ×0.757λ)*
This work	5	1.00-2.58	88.04 %	0.397 λ × 0.377 λ

*size of these reflectometers are calculated using 3 mm length for the TL with 50 ohm impedance.

This paper proposes a new triple-ring symmetric FPR with fractional bandwidth of 85%, which is 12% improvement over best design existing in [16]. The improvement is led by our proposed technique called triple-ring based fully shifted design topology where 36° angular displacement between tapered inter-ring sections and matching arms are maintained to produce additional electrical length. Moreover, a miniaturization is achieved by curving TL in the matching sections with angular bend, resulting total dimensions of $0.397\lambda \times 0.377\lambda$. Measured results demonstrate bandwidth from 0.96 GHz to 2.38 GHz with a reflection coefficient below -20 dB, and a -6 ± 1 dB transmission coefficient with the required phase shift of $\pm120°$ between ports. To the best of our knowledge, such bandwidth is the widest to be achieved in literature thus far for a symmetric FPR. The rest of the paper is presented as follows: Section II discusses the theory along with the architecture of the proposed design followed by the results in Section III. Section IV briefly describes the general procedure of brain microwave imaging system with the proposed FPR and Section V concludes the paper.

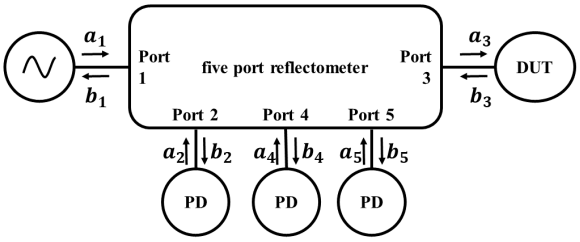

FIGURE 1. Five-port reflectometer: illustrative demonstration.

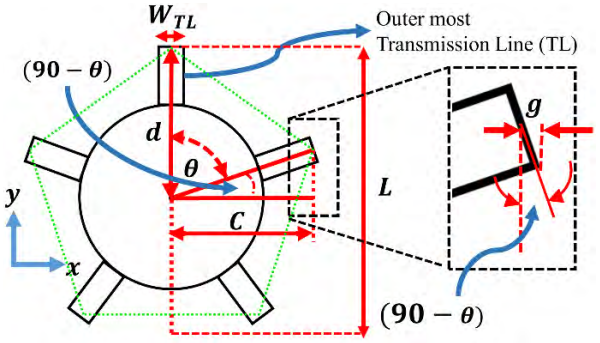

FIGURE 2. Measurement of size of five-port reflectometer.

II. FIVE-PORT REFLECTOMETER: THEORY, MEASUREMENT OF SIZE, AND PROPOSED DESIGN

A. THEORY

In FPR, one port is generally dedicated for the signal source and another one for the DUT, as shown in Fig. 1. Other ports are connected to power detectors. The waves entering to and emerging from the reflectometer are denoted as a_i, b_i, ($where\ i = 1, 2, \ldots, 5$), respectively. In the case of a symmetric reciprocal FPR, the coupling properties can be explained using the relationship between S-matrix eigen vectors (S_1, S_2, S_3) and three independent eigen elements $S_{11}\ (= S_{22}, S_{33}, S_{44}, S_{55})$, $S_{12}\ (= S_{15})$, $S_{13}\ (= S_{14})$ [17], [30], [31]. These three elements are represented as γ, α, and β, respectively, based on the generic form of the S-matrix derived in [16]. Parameter γ denotes the reflection coefficient characteristics ($S_{ii}(i = 1, 2, .., 5)$), whereas α and β represent the transmission coefficient characteristics ($S_{ij}; i, j = 1, 2 \ldots, 5 (i \neq j)$). Applying the condition of a lossless matched junction, the following properties can be derived [14], [30]:

$$|\gamma| = 0\ (< -20\ \text{dB})^* \tag{1}$$

$$|\alpha| = |\beta| = 0.5\ (-6 \pm 1\text{dB})^* \tag{2}$$

$$\angle\alpha = \angle\beta \pm 120^\circ \tag{3}$$

It is difficult to fulfill the required $\gamma = 0$ over a broad bandwidth, and a tolerance value of -20 dB (marked with asterisk in (1)) is considered as threshold value in the broadband design, as described in [15] and [17]. The magnitude and phase characteristics of the coupling, α and β (shown in (2) and (3)) are related to the magnitude of reflection coefficient ($|\gamma|$) [17]. This confirms that the -20 dB tolerance for γ will satisfy the coupling characteristics as well. However, to ensure additional accuracy, a tolerance of only ± 1 dB in terms of coupling is set when optimizing the structure using Advanced Design System (ADS) as indicated by asterisk in (2).

B. SIZE CALCULATION FOR PLANAR MULTI-PORT REFLECTOMETERS

In the case of symmetric single ring multi-port reflectometers, the general design procedure includes one central ring with n-number of arms extending outwards from that central ring. Alternatively, in the case of multi-ring multi-port reflectometers, these arms are extended from the outer-most ring, consisting of fixed inter-port physical angular displacements of $\theta = (360/n)$. This forms a polygonal shape of the reflectometer (pentagonal for FPR (with $n = 5$), as illustrated in Fig. 2 (green dotted line)). The sizes of the symmetric multi-port reflectometers in [11] and [32] and FPRs in [13]–[17] are presented in terms of the individual dimensions of the transmission lines (for instance, [13, Table 2] and [32, Table 1]). Therefore, there remains a need of standardized method to compare the overall sizes of these multiport (with $n \geq 4$) reflectometers. This is to ensure proper size comparison of these structures, which is presented as follows.

Let $n(\geq 4)$ be the number of ports in the symmetric planar reflectometer. Each of the ports is mutually displaced with an angle of $\theta = (360/n)$ from each other (for the case of FPR, $\theta = 72^\circ$). The distance between the midpoint of the width of outermost TL arm, W_{TL}, (typically designed with an impedance of 50 Ω or 70 Ω) and the center of the polygon is defined as d. Meanwhile, the approximate length of the overall structure (L) is deduced to be twice of the length d, based on (4). Half of the width (along the x-axis in Fig. 2) of the overall polygonal structure (pentagonal in the case of FPR), can be calculated by adding C and g, as illustrated in Fig. 2. The value of C is equal to $d \times \sin\theta$, whereas the value of g can be written as $\frac{W_{TL}}{2} \times \cos\theta$. The total width can finally be calculated using (5), as follows:

$$L = 2 \times d \tag{4}$$

$$W = 2 \times (C + g) = 2 \times (\text{d} \times \sin\theta + \frac{W_{TL}}{2} \times \cos\theta) \tag{5}$$

Using the value of $\theta = 72^\circ$, the calculated width of FPR is $W = (1.9\, d + 0.3 W_{TL})$. Equations (4) and (5) can be used to categorize the literatures related with symmetric multi-port reflectometers in terms of size as it is done in Table 1 of this manuscript.

C. DESIGN METHODOLOGY

The proposed design features a novel scheme with the inclusion of triple rings and tapered inter-ring transmission lines

*mark represents the threshold value to be maintained in broadband design.

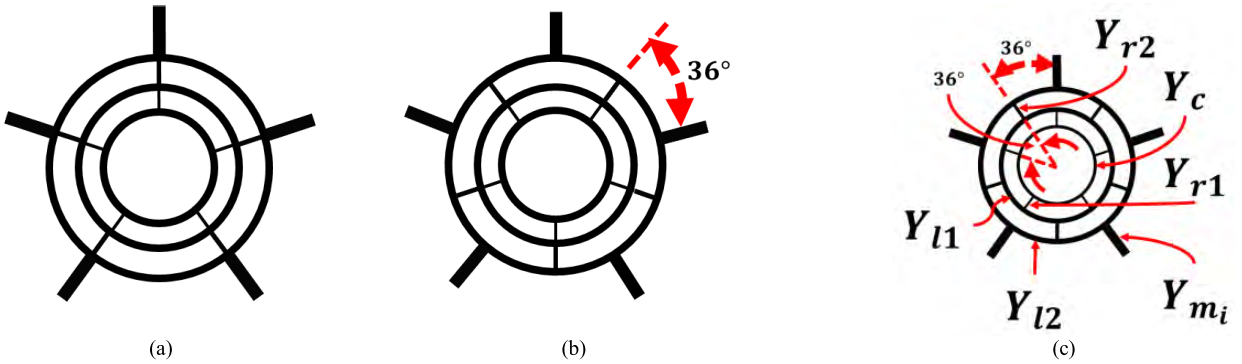

FIGURE 3. Overview of the design flow for the proposed triple ring-based FPR: (a) non-shifted (b) partially shifted (c) fully shifted design architecture.

TABLE 2. Parameter list for different optimization steps for triple ring non-shifted design (Fig. 3(a)).

Sections		Optimization 1		Optimization 2		Optimization 3		Optimization 4	
Description	Symbol	Width (mm)	Length /λ_g	Width (mm)	Length /λ_g	Width (mm)	Length /λ_g	Width (mm)	Length /λ_g
1st ring	Y_c	1.040	0.1162	1.0750	0.123	1.04	0.1431	1.04	0.0799
1st inter-ring TL	Y_{r1}	7.143	0.0447	6.0742	0.0226	9.3772	0.0391	6.366	0.0317
2nd inter-ring TL	Y_{r2}	4.617	0.1016	4.299	0.06	2.7861	0.0602	5.0523	0.06
1st matching section	Y_{m1}	3.010	0.1802	3.1047	0.14	2.9194	0.1843	3.8053	0.1077
2nd matching section	Y_{m2}	1.517	0.1359	1.6029	0.1721	N/A	N/A	1.9121	0.1072
2nd ring	Y_{l1}	1.351	-	1.0276	-	0.1558	-	0.5182	-
3rd ring	Y_{l2}	0.236	-	0.7303	-	0.277	-	0.3206	-

*$\lambda_g = 202.2$ mm

as stated earlier. The target operating band has been chosen between 1 and 4 GHz.

1) EVOLUTION OF FULLY SHIFTED DESIGN WITH TAPERED INTER-RING TRANSMISSION LINE

The design is realized in planar microstrip technology and comprises of three concentric rings (as opposed to two rings in [16], [17], and [26]) with five arms expanding outwards, with a mutual angular distance of $\theta = \left(\frac{360°}{5}\right) = 72°$. The angular distance ensures equal power division so that the 4-way power divider property can be accomplished (i.e., $S_{12} = S_{15}$ and, $S_{13} = S_{14}$). The second and third concentric ring (considering from center towards the periphery of the design) act as compensating network for broadband design, based on mutual coupling between adjacent ports. The longer electrical length of the outer rings (due to longer periphery) corresponds to the addition of some lower frequency zone in the overall functional bandwidth of the reflectometer. Each ring is connected with the subsequent ring through inter-ring TLs. Fig. 3 depicts a design flow of proposed triple-ring based fully shifted architecture adopted in this research. The design flow is based on shifting of inter-ring transmission lines from the hypothetical axis line passing through the arms and the center of the concentric rings (see Fig 3(b)). The shifting arrangements of the first two design architectures namely, (i) non-shifted (Fig. 3(a)) and (ii) partially shifted architectures (Fig 3(b)) are adopted in five-port reflectometers in literatures; however, with two rings (see [16] and [17] respectively). In this research, we have investigated possible design with three rings as increasing the number of rings has been proven to be effective in broadband design from other literatures. The radii of curved TLs in 1st, 2nd, and 3rd rings are denoted by R_{Y_c}, $R_{Y_{l1}}$ and $R_{Y_{l2}}$, respectively. In non-shifted design architecture (Fig. 3(a)), the inter-ring TLs and outer arms are in same hypothetical line (Fig. 3(b)), whereas in partially shifted architecture, the inter-ring TLs are shifted from the outer arms by an angular displacement of 36° (Fig. 3(b)). Four different optimizations have been performed in non-shifted architecture to surpass the reported bandwidth (see Table 2 for detail). However, both of first two design architectures failed to achieve higher bandwidth than the existed literature; therefore, we have designed fully shifted architecture. Our design architecture comprises of fully shifted arrangement as depicted in Fig. 3(c). It can be seen that the proposed fully shifted architecture comprises additional relative shifting of 36° between two consecutive inter-ring TLs, Y_{r1} and Y_{r2}. Therefore, there are two levels of shifting in this architecture: (i) from first inter-ring TL, Y_{r1}, to second inter-ring TL, Y_{r2} and (ii) from second inter ring TL, Y_{r2}, to the arms of FPR. This two-level

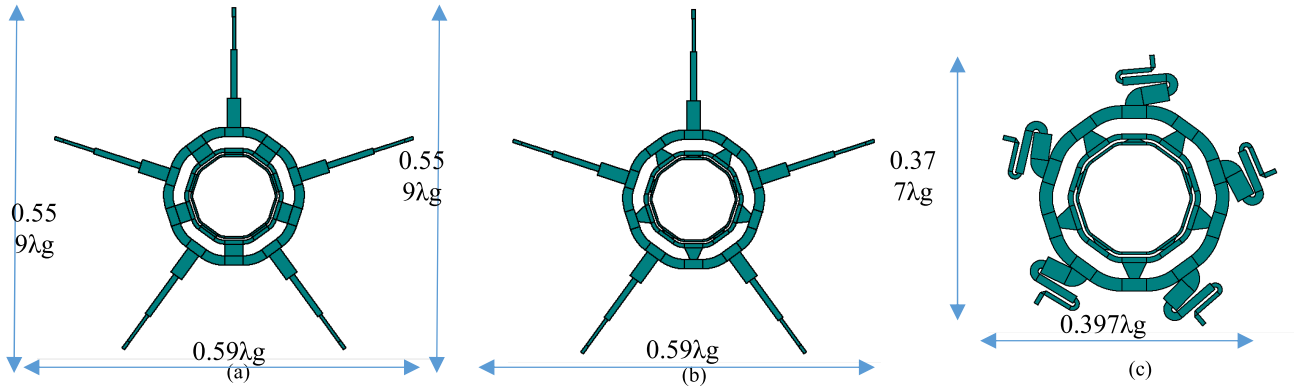

FIGURE 4. Different fully shifted sub-topologies: (a) without tapered inter-ring TL (non-compact), (b) with tapered inter-ring TL (non-compact), and (c) final design: with tapered inter-ring TL (compact).

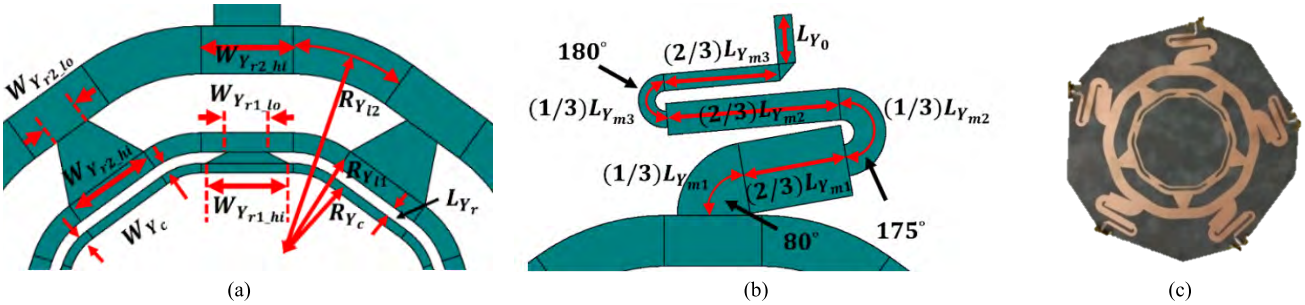

FIGURE 5. Descriptive view of final design in 4(c): (a) inner rings (b) outer matching arms (c) Fabricated prototype.

shifting arrangement provides additional electrical length to the inter-port transmission signals. The designs in [11] and [26] may appear to be same with this design in terms of shifting, however those designs are based on star-ring topology whereas we are focusing on ring topology. To be specific, we have introduced another ring in the middle of the designs in [11] and [26]. Moreover, those designs are proposed for six-port reflectometer. The reason of choosing five-port reflectometer has been described in Section I. The comparative details of different electric lengths introduced in different shifted architectures will be discussed in Section III. It can be summarized from the investigation of shifted architectures that if more inter-ring TLs are introduced with mutual angular displacement equivalent to factors of 72°, such as 9°, then further broader bandwidth can be achieved while maintaining the same number of rings.

Tapered transmission matching arms has been used in previous FPRs and SPRs [16], [26]. However, as it is hard to achieve bended tapered TL to provide size compactness, we have chosen it to be used in inter-ring sections for the first time, while we have designed bended matching sections which will be discussed soon. To investigate the effect of tapered inter-ring TLs, we have designed two types of sub-topologies in the triple-ring fully shifted design namely: (i) without tapered TL in inter-ring sections Y_{r1} and Y_{r2} (Fig. 4 (a)) (ii) with tapered TL in inter-ring sections Y_{r1} and Y_{r2} (Fig. 4 (b)). The demonstration of the effect of tapered TLs along with the effect of shifting is performed by assigning the same length and width for each constituting section in both partially shifted and fully shifted designs (presented in Table 3). The descriptive effect of tapered TLs will be presented in Section III. The wider parts of the tapered TLs used in first and second inter-ring sections (Y_{r1} and Y_{r2} respectively) in proposed design are denoted as $W_{Y_{r1\_hi}}$ and $W_{Y_{r2\_hi}}$ respectively, while the narrower parts are denoted as $W_{Y_{r1\_lo}}$ and $W_{Y_{r1\_lo}}$ (Fig. 5 (a)). In the case of the designs without tapered TLs (partially shifted and 1st sub-topology of fully shifted design), the widths of the inter-ring sections, Y_{r1} and Y_{r2}, are maintained at the same value of $W_{Y_{r2\_hi}}$. Least-squares error function (EF)-based (shown in (6))

TABLE 3. Parameter description for partially and fully shifted design.

Parameter	Value ($*\times \lambda_g$)	Parameter	Value (mm)	Parameter	Value (mm)
$L_{Y_{r1}}$	0.006	R_{Y_c}	6.929	$W_{Y_{r1\_lo}}$	4.363
$L_{Y_{r2}}$	0.0319	$R_{Y_{l1}}$	9.868	$W_{Y_{r2\_hi}}$	10.14
$L_{Y_{m1}}$	0.08	$R_{Y_{l2}}$	20.15	$W_{Y_{r2\_lo}}$	4.114
		W_{Y_c}	1.04	L_{Y_0}	3
$L_{Y_{m2}}$	0.1327	$W_{Y_{m1}}$	7.36	W_{Y_0}	1.81
		$W_{Y_{m2}}$	3.259	$W_{Y_{l1}}$	2.140
$L_{Y_{m3}}$	0.0890	$W_{Y_{m3}}$	1.724	$W_{Y_{l2}}$	5.245
		$W_{Y_{r1\_hi}}$	9.172	λ_g	202.2

genetic algorithm in ADS has been used for global search to optimize the design. Upon obtaining the global value, Quasi-Newton optimizer has been used as local optimizer, which uses Davidson-Fletcher-Powell (DFP) formula to estimate the new value in each iteration [33].

$$EF = \sum_{m}^{M} W_\gamma \times |\gamma\,(f_m)|^2 + W_\beta \times \left[|\beta\,(f_m)| - \frac{1}{2}\right]^2 + W_\alpha \times \left[|\alpha\,(f_m)| - \frac{1}{2}\right]^2 \quad (6)$$

In (6), m denotes the start frequency of the optimization and M denotes the stop frequency, W denotes weighting factor for optimization. Rogers RT/Duroid 5880 ($\varepsilon_r = 2.2$) has been used to validate the design.

2) MINIATURIZATION OF THE DESIGN

The miniaturization of the fully shifted design with tapered inter-ring TL is achieved using curved configuration of the three matching TLs Y_{m1}, Y_{m2} and Y_{m3} while maintaining the same electrical length. This compact design is shown in Fig. 4 (c) while a detailed view is presented in Fig. 5. In compact design, each of the three matching sections is divided into two parts: (i) curved sections with a third of the required length (denoted as $\left(\frac{1}{3}\right)L_{Y_{m1}}, \left(\frac{1}{3}\right)L_{Y_{m2}}, \left(\frac{1}{3}\right)L_{Y_{m3}}$ in Fig. 5 (b)) and (ii) straight sections with two third of the required length denoted as $\left(\frac{2}{3}\right)L_{Y_{m1}}, \left(\frac{2}{3}\right)L_{Y_{m2}}, \left(\frac{2}{3}\right)L_{Y_{m3}}$ in Fig. 5 (b)). The radii of the curved TLs are calculated as follows:

$$R_{Y_{mi}} = \frac{\frac{L_{Y_{mi}}}{3}}{\frac{(angle)_i}{180}\pi} \quad (i = 1, 2, 3) \quad (7)$$

In (7), the value i represents the number of the matching section, $L_{Y_{mi}}$ denotes the length of the corresponding matching section, and $(angle)_{1,2,3} = 80°, 175°, 180°$ respectively. The values of these angles are chosen to ensure maximum reduction of the size without hampering the easiness of fabrication. This design has shown improved bandwidth fulfilling the criteria of $\gamma < -20\ dB$. Following the general convention of broadband design, the −20 dB port insertion loss condition [16], [17] has been met, with a −6±1 dB for port to port couplings. The fabricated prototype is shown in Fig. 5 (c).

III. RESULTS AND DISCUSSION

Table 4 shows the results of optimizations for the non-shifted design which is a preliminary design of proposed FPR. In several consecutive steps of optimization, a broadband design with a fractional bandwidth of 99.34 % (optimization 4) which fulfills $\gamma < -10$ dB is achieved. However, the highest bandwidth below −20 dB for this design is only 24.4 % (from 0.795 GHz to 1.016 GHz) for optimization 1. For this reason, other shifted topologies (depicted by Fig. 6) are investigated with additional shifted arrangements based on physical angular displacement ($\partial\theta_a$) and electrical length (θ_e) of inter- port transmission signal components. In the case of transmission signal component through the 1st ring, partially shifted design (Fig. 6(d)) and fully shifted design (Fig. 6(g)) have introduced additional electrical length of $0.124\boldsymbol{\lambda_g}$ and $0.184\boldsymbol{\lambda_g}$ respectively, compared to non-shifted design (Fig. 6(a)). However, in the case of 2nd ring, partially shifted (Fig. 6(e)) and fully shifted design (Fig. 6(h)), both have additional electrical length of 0.124 $\boldsymbol{\lambda_g}$ compared to the non-shifted (Fig. 6(b)). It can be seen that in the case of 3rd ring, the transmission signal component travels same electrical length ($0.753\lambda_g$) in each of the designs. The value of λ_g is 202.2 mm, as used in previous calculations. The reflection coefficient results for different shifted designs are presented in Fig. 7 for the port 1. These results are presented in more details in Fig. 8(a) and Table 5. Other ports have similar bandwidth due to reciprocal symmetry, as can be seen from Fig. 8(b)-8(e), which confirms the criterion in Eq. (1). For the partially shifted design, the bandwidth is 41.64 % in comparison to 24.4 % for non-shifted design, which again proves the contribution of shifted design in broadband symmetric ring junction, as suggested in [11] and [16]. Moreover, from the bandwidth comparison between partially and fully shifted designs, another conclusion can be drawn - if the shifted design has no mutual shift between the inter-ring TLs, then the highest bandwidth will not be achievable for the triple ring based FPR. For the fully shifted design, there is additional electrical length (Fig. 6 (bottom row)) which enhances the operational bandwidth. Fully shifted topology with tapered TLs has managed to improve matching between the consecutive rings. All these mechanisms work together to increase the bandwidth of the proposed design from the state of the art FPRs. Therefore, the

TABLE 4. Simulated bandwidth (with $\gamma < -20$ dB) for different optimizations of the non-shifted design (based on parametric values presented in table 2).

Optimization	Frequency band (<-20 dB)	BW_{-20dB} (%)
Optimization 1	0.795-1.016	24.4
	1.349-1.527	12.37
Optimization 2	0.961-1.064	10.17
	1.898-2.058	8.089
Optimization 3	0.770-0.961	0.039
	1.846-1.905	3.15
Optimization 4	2.644-2.775	4.835

TABLE 5. Simulated bandwidth (with $\gamma < -20$ dB) for the partially shifted (Fig. 3 (b)) and different variations of the fully shifted design (Fig. 4).

Topology	BW_{-20dB} (%)	Frequency range (GHz)
Partially shifted	41.64	0.987-1.506
Fully shifted without taper (non-compact)	48.29 & 7.34	0.986-1.608 & 2.196-2.363
Fully shifted with taper (non-compact)	88.96	0.996-2.592
Compact Fully shifted with taper	88.04	1.004-2.583

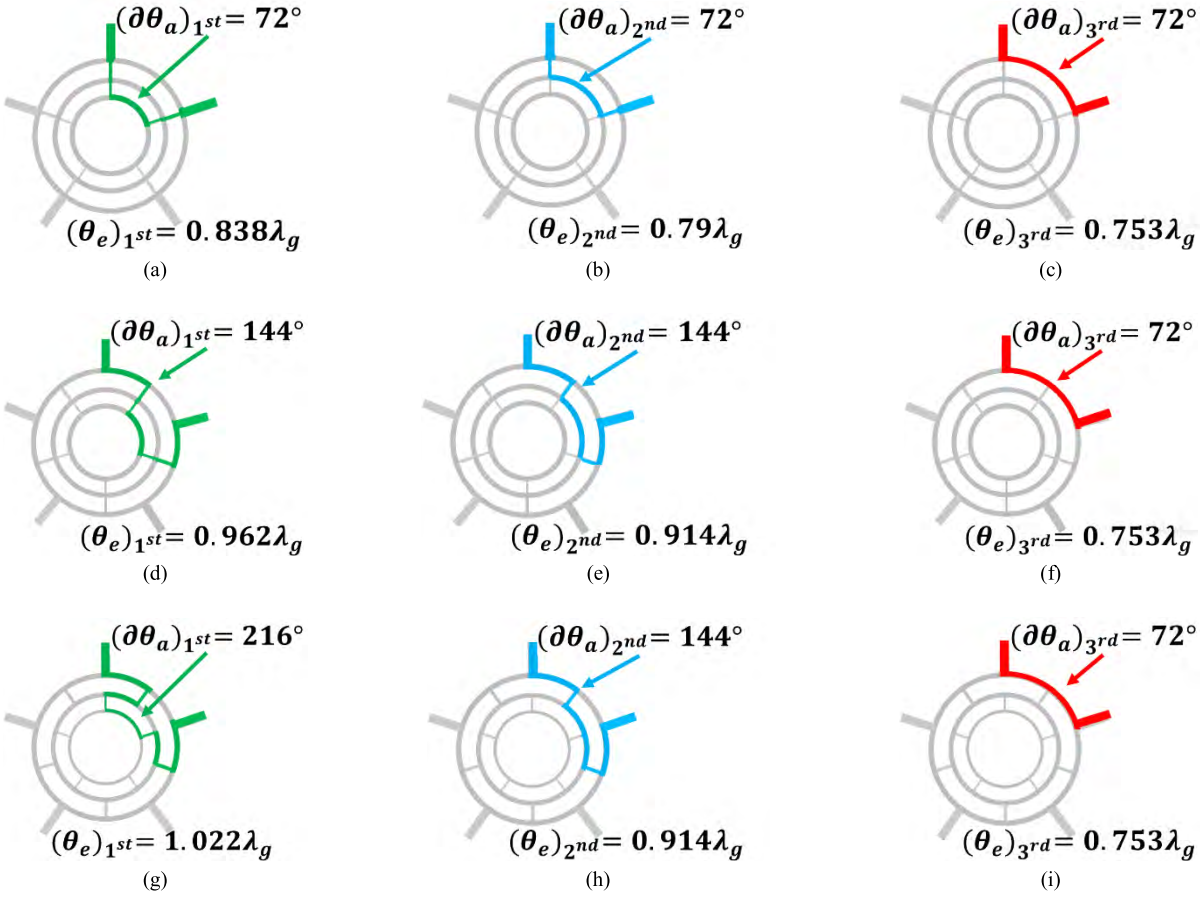

FIGURE 6. Electrical length for inter-port transmission signal components through the 1st, 2nd and 3rd ring for the non-shifted design (top row), partially shifted design (middle row), and the fully shifted design (bottom row).

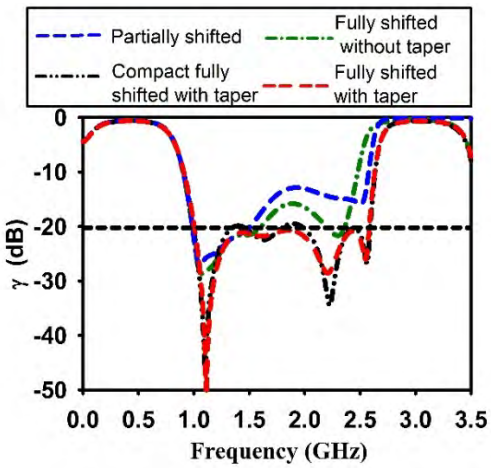

FIGURE 7. Reflection coefficient bandwidth (with $\gamma < -20$ dB) for the partially shifted (Fig. 3 (b)) and different variations of the fully shifted design (Fig. 4) (details of the bandwidth are presented in Table 5).

bandwidth increases to 48% for fully shifted design without tapered TLs.

The introduction of tapered TLs has increased the bandwidth up to 90% in simulation. Bandwidth is slightly dropped to 88% in the compact design due to the discontinuity effect of the curved sided TLs introduced at matching arms. Nonetheless the physical size of the proposed FPR has been reduced to $0.59\lambda_g \times 0.559\lambda_g$ in comparison with $1.029\lambda_g \times 0.98\lambda_g$ which is without the curved TLs at the wavelength corresponding to 1 GHz. Therefore, 43% reduction in length and 43% in width of overall size of proposed FPR have been achieved due to the presence of curved TLs in the matching arms. The simulated and measured reflection coefficients are shown in Fig. 8. The measurement has performed using Agilent E5071C ENA. It can be seen that the proposed FPR has featured higher fractional bandwidth than [16] and [17]. Meanwhile, Fig. 9(a) and 9(b) depict the magnitudes and phases of the transmission coefficients related with port 1. In Fig. 8 and 9(a), the shaded zones represent the band with $\gamma < -20$ dB characteristics. Measured bandwidth of proposed FPR is 87.43 % (from 0.94 to 2.4 GHz), 86.75 % (from 0.94 to 2.38 GHz), 87.43 % (from 0.94 to 2.4 GHz), 85.04 % (from 0.96 to 2.38 GHz), and 87.76 % (from 0.94 to 2.41 GHz) for port 1 to port 5 respectively. Meanwhile, the same 88.04 % of fractional bandwidth is obtained at all ports due to the ideal conditions in simulations. For the sake of brevity, only port 1 is shown in Fig. 9(a) and 9(b).

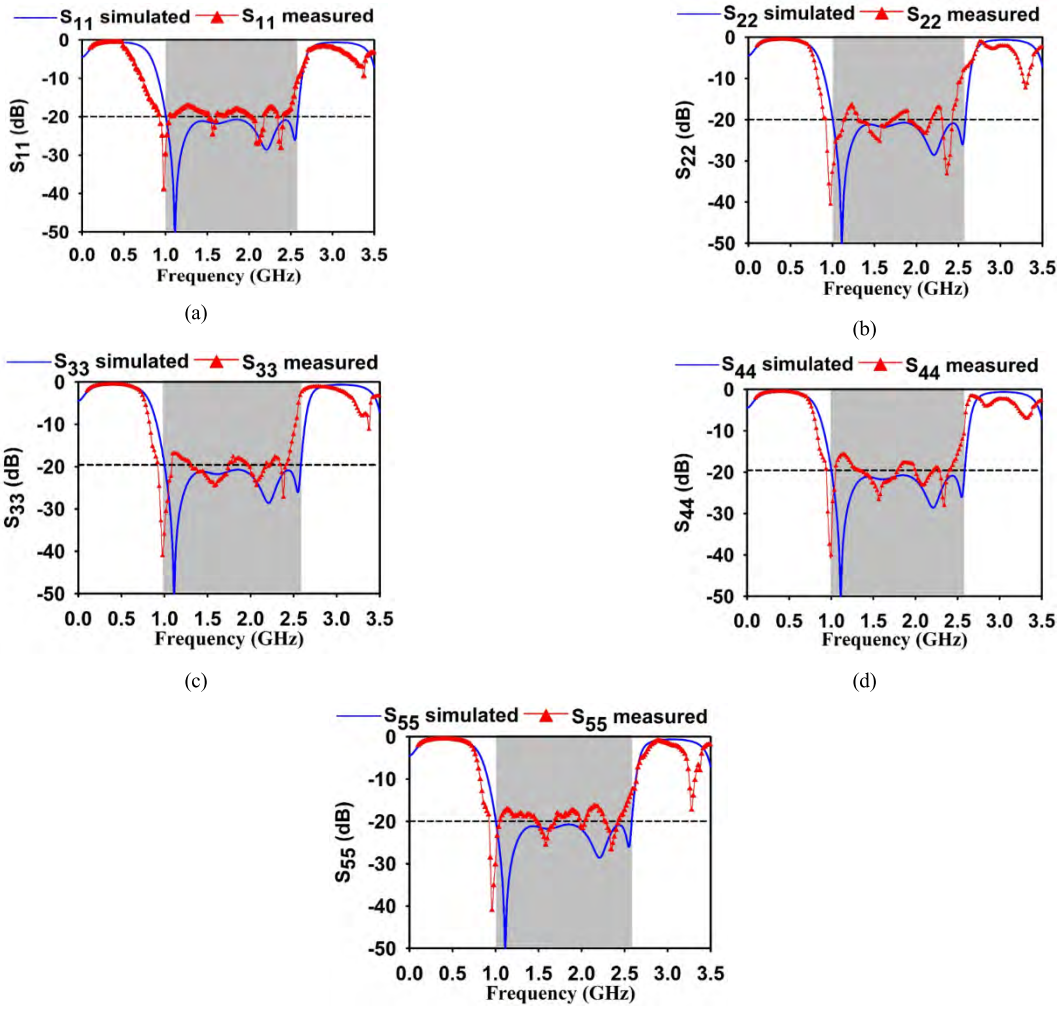

FIGURE 8. Simulated and measured results of reflection coefficients of different ports. (a) port 1, (b) port 2, (c) port 3, (d) port 4, and (e) port 5.

Besides that, since $S_{12} = S_{15}$ and $S_{13} = S_{14}$, only S_{12} and S_{13} are presented in Figs. 9(a) and 9(b). The characteristics of the FPR depends on the matching of the junction as described in [17]. In bands where there exist mismatch and deviation from the simulated insertion loss, the transmission characteristics (both phase and magnitude) are also deviating from the desired values in these regions. It can be seen from Fig. 9(a) that the proposed FPR has met the four-way equal power dividing criterion (as in (2)). This means that the port 1 has successfully divided 25 % of input power to each of the other four ports to stabilize coupling and increase matching of minimum -20 dB reflection loss. The stabilization of -6 dB coupling for each port is crucial as FPR will not be functioning well if any inconsistency of input power is detected among the ports. Such principal is different compared to other microwave components like front-end antennas where matching can be increased by reducing mutual coupling as stated in [34]. Measured transmission coefficients indicate a mean absolute deviation of 0.031 and 0.018 from the simulated values for S_{12} and S_{13}, respectively. Due to symmetry, the other ports have similar characteristics in terms of mutual coupling. Even though the reflection coefficients with less than -20 dB will also ensure that the phase characteristics have met the criterion presented in (3), the phase differences at four specific frequencies are also presented in Table 6 for further validation. These frequencies are chosen from the notches with higher matching in the reflection coefficients shown in Fig. 8(a). For measurements, slightly different frequencies are selected and presented in Table 6 due to the frequency shift relative to simulations. The phase differences are calculated between S_{12} and S_{15} for the first case, and between S_{13} and S_{14} in the second case. It is seen, within those notches, the phase differences vary by about $\pm 5^\circ$ from the ideal value of 120° or 240°. Meanwhile, throughout the whole measured operating band (from 0.94 GHz to 2.41 GHz), the phase difference fulfilled the criterion required by (3),

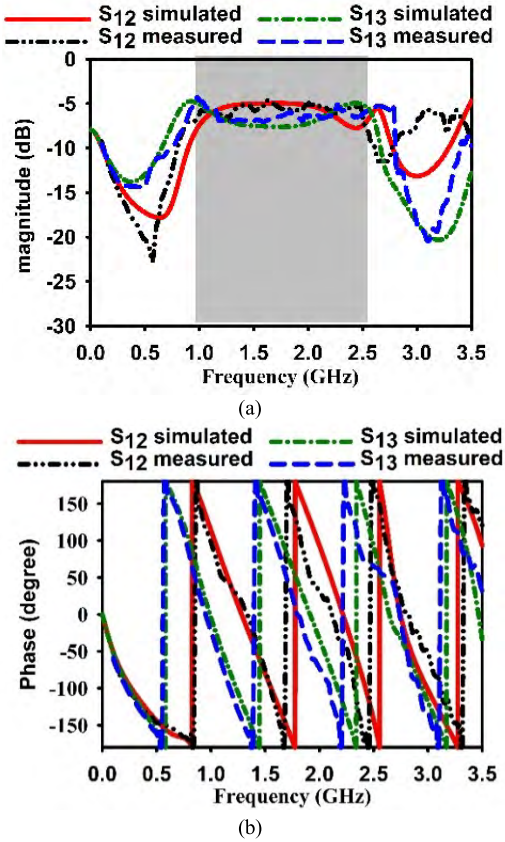

FIGURE 9. Simulated and measured transmission coefficients (a) Magnitude (dB) (b) phase.

TABLE 6. Phase characteristics for the transmission coefficients relative to Port 1.

Freq. (GHz)		Phase (°)				Phase Difference
		$\angle S_{12}$	$\angle S_{15}$	$\angle S_{13}$	$\angle S_{14}$	
Simu.	1.11	67.6		-52.7		120.3
Meas.	0.98	107.4	109.9	-12.5	-7.3	119.9 & 117.2
Simu.	1.61	-119.7		117.8		237.5
Meas.	1.66	-163.8	-164.2	69.5	83.3	233.3 & 247.5
Simu.	2.21	3.8		-117.8		121.6
Meas.	2.11	5.2	-4.5	-115.4	-132.5	120.6 & 128
Simu.	2.55	-177.2		62.7		239.9
Meas.	2.4	-168.5	-169.9	75.3	75.9	243.8& 245.8

resulting in values of 120° or 240°, as observed in Fig. 10. It can be seen that there is a slight deviation between two graphs between the range of 2.2 and 2.5 GHz. The shift is due to the deviation of measured reflection coefficients (as can be seen in Fig. 8) since the transmission coefficient is influenced by reflection coefficient of FPR as mentioned in [17]. Ultimately, the proposed FPR fulfills the three main criteria specified in (1) to (3), and has featured measured bandwidth of at least 85 %. This fractional bandwidth, along with the coupling characteristics indicate its potential as a cost-effective, portable microwave imaging-based solution for a brain injury diagnosis system, whose description is coming in Section IV.

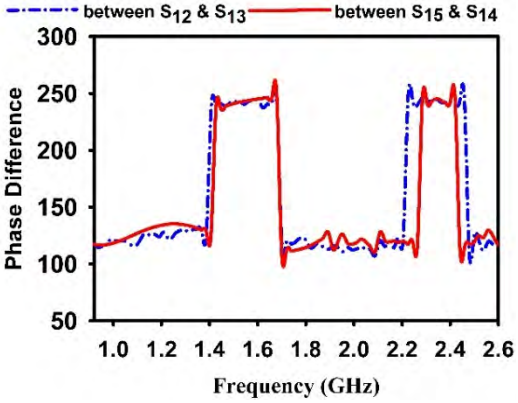

FIGURE 10. Measured phase difference between transmission coefficients related to port 1.

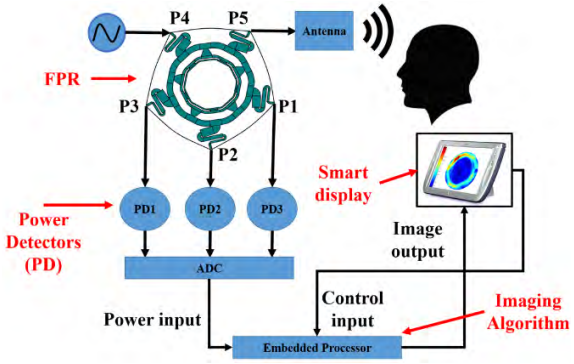

FIGURE 11. Portable brain injury diagnosis system incorporating the proposed FPR.

IV. FPR-BASED BRAIN MICROWAVE IMAGING SYSTEM

A. SYSTEM SETUP

The general architecture of the proposed imaging system and the integration of the proposed FPR is shown in Fig. 11. A portable programmable microwave signal generator (Mini Circuit's) will be connected to port 1 (P1), whereas port 5 (P5) will be connected to a wideband antenna. The other three ports (P2, P3, P4) will be connected to diode power detectors. The antenna will be excited using very low, 1mW (0 dBm) power to ensure minimal radiation effect on the subject (patient) [35]. The detected signal power will be converted into the digital form using an analog to digital converter (ADC). This is set as input to the reflection coefficient measurement algorithm (coded with LabVIEW) embedded in the processor, myRIO. The antenna will be rotated around the head phantom using a stepper motor-controlled platform (see Fig. 12). Each sub-components of the system will be controlled using a LabVIEW-based GUI. For each frequency sample f and each antenna position $\overline{v_k}$ $(f, k \in \mathbb{N})$ (see Fig.12), the complex reflection coefficient matrix $\Gamma(f, k) \in \mathbb{C}$ will be calculated from the detected power according to the description in the Section B.

B. MEASUREMENT OF $\Gamma(j,k)$

The programmable imaging system is initialized with the insertion of the start and stop frequencies (F_{lo}, F_{hi}), total number of frequency sampling points, F, output signal level, and the total number of points for the antenna rotation around the head, K. Next, the FPR will be calibrated using different calibration standards – a 50 Ω matched load standard, an open standard, and two other open offset standards (120° and 240°). The following derivation process will be used to evaluate the reflection coefficients (Γ_i) of the antenna.

$$\frac{P_i}{A_i} = |\Gamma_i - q_i|^2 \tag{8}$$

$$\Gamma_i = u_i + jv_i \tag{9}$$

$$q_i = x_i + jy_i \tag{10}$$

where $i = 2, 3, 4$ representing the port number which is to be calibrated, while P_i and Γ_i are the detected power and reflection coefficient at port i. Meanwhile, A_i and q_i are complex constants which will be calculated using the transformations shown in (12). The calibration standards are denoted as $o(0)$, ma, $o(120)$, $o(240)$ for open, match, open with 120° offset and open with 240° offset respectively. For example, the match load calibration standards used at port 2 shown in (11), as shown at the bottom of this page, can be derived from equations (8) to (10). Upon the evaluation of (11) for each of the calibration standards, followed by further simplifications, the resultant matrix shown in (12), as shown at the bottom of this page, can provide the values of A_2, x_2 and y_2. The values of A_i, x_i and y_i in (8) can be used to determine the reflection coefficient ($\Gamma = U + jV$) of the antenna (at port 5, see Fig. 11) using (13), as shown at the bottom of this page. This process will be repeated for each frequency to generate the one-dimensional (1D) matrix $\Gamma(f)$. According to the value of K, the system will automatically move to the next antenna position to generate a two dimensional (2D) frequency domain matrix $\Gamma(f, k)$ [36].

C. IMAGE CONSTRUCTION

The head imaging scenario has been depicted in Fig. 12. $\bar{w}_r(x_r, y_r)$ $(r = 1, 2, \ldots R)$ are the points on the head-skin interface boundary. The generated frequency domain reflection coefficient matrix, $\Gamma(f, k)$ will be converted into time domain $\zeta(t, k)$using the inverse Fourier transform. A confocal microwave imaging algorithm will then implemented as discussed in [37]. In this stage, the effects of the reflection from the background will be removed by subtracting $\zeta(t, k-1)$ (signal form adjacent antenna (k−1)), from $\zeta(t, k)$, resulting in the calibrated signal $\zeta(t, k)_{calibrated}$ as shown in (14) [38].

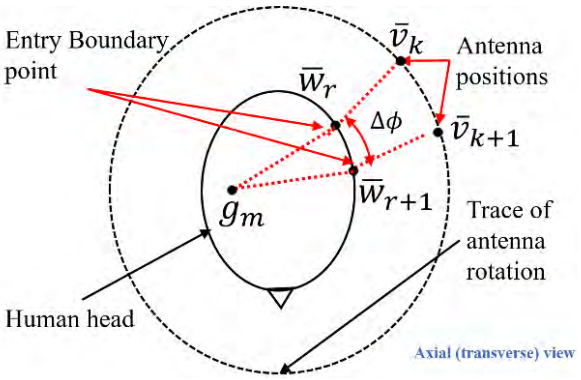

FIGURE 12. Depiction of imaging around the head process.

$$\zeta(t, k)_{calibrated} = \zeta(t, k) - \zeta(t, k-1) \tag{14}$$

This is followed by the hypothetical division of the imaged region into m ($m \in \mathbb{N}$) number of smaller imaging cells, $\bar{g}_m$ (see Fig. 12), with coordinate specification (x_m, y_m) [39]. Next, the propagation time of the signal traversing from the antenna at position k to the imaging cell, $\tau(g_m, k)$ will be calculated using (15). This is calculated according to Fermat's principle, and estimates the minimum time for the signal to travel from the antenna to g_m through R possible entry points at the boundary (see Fig. 12) [20], [37], [38].

$$\tau(g_m, k) = \min_{g_m}\left[\frac{||\bar{v}_k - \bar{w}_r||}{c} + \frac{\sqrt{\varepsilon_{head}}\,||\bar{w}_r - \bar{g}_m||}{c}\right] \tag{15}$$

where, ε_{head} is the average permittivity of the head while c is the velocity of the light in free space. Using a delay-and-sum (DAS) algorithm, the intensity value corresponding to each imaging cell g_m can be used to generate the image of that

$$\frac{P_{2_{ma}}}{A_2} = u_{2_{ma}}^2 - 2u_{2_{ma}}x_2 + x_2^2 + v_{2_{ma}}^2 - 2v_{2_{ma}}y_2 + y_2^2 \tag{11}$$

$$\begin{bmatrix} u_{2_{ma}}^2 - u_{2_{o(0)}}^2 + v_{2_{ma}}^2 - v_{2\_o(0)}^2 \\ u_{2_{ma}}^2 - u_{2_{o(120)}}^2 + v_{2_{ma}}^2 - v_{2\_o(120)}^2 \\ u_{2_{ma}}^2 - u_{2_{o(240)}}^2 + v_{2_{ma}}^2 - v_{2_{o(240)}}^2 \end{bmatrix} = \begin{bmatrix} P_{2\_o(0)} - P_{2_{ma}} & 2(u_{2_{ma}} - u_{2_{o(0)}}) & 2(v_{2_{ma}} - v_{2_{o(0)}}) \\ P_{2\_o(120)} - P_{2_{ma}} & 2(u_{2_{ma}} - u_{2_{o(120)}}) & 2(v_{2_{ma}} - v_{2_{o(120)}}) \\ P_{2\_o(240)} - P_{2_{ma}} & 2(u_{2_{ma}} - u_{2_{o(240)}}) & 2(v_{2_{ma}} - v_{2_{o(240)}}) \end{bmatrix} \begin{bmatrix} \frac{1}{A_2} \\ x_2 \\ y_2 \end{bmatrix} \tag{12}$$

$$\begin{bmatrix} \frac{P_2}{A_2} - \frac{P_3}{A_3} - x_2^2 + x_3^2 - y_2^2 + y_3^2 \\ \frac{P_3}{A_3} - \frac{P_4}{A_4} - x_3^2 + x_4^2 - y_3^2 + y_4^2 \end{bmatrix} = \begin{bmatrix} U \\ V \end{bmatrix} \begin{bmatrix} 2(x_3 - x_2) + 2(y_3 - y_2) \\ 2(x_4 - x_3) + 2(y_4 - y_3) \end{bmatrix} \tag{13}$$

cell [20], [37], [38], [40]:

$$I = \sum_{k}^{K} \left[\left(\zeta \left(t, k \right)_{calibrated} \right) . \left(2\tau \left(g_m, k \right) \right) \right]^2 \qquad (16)$$

V. CONCLUSION

A symmetric broadband microstrip five-port reflectometer has been proposed. Different topologies have been assessed using parametric study, and a triple ring-based fully shifted configuration with tapered inter-ring TLs has been chosen as the final prototype. The proposed FPR has featured a measured bandwidth of at least 85 % (with at least -20 dB of reflection coefficient), sized at $0.397\ \lambda_g \times 0.377\lambda_g$. Besides that, a standardized method in assessing the overall size of different reflectometers with more than four ports is also presented to ease comparison of the proposed FPR with literature. The measured phase characteristics vary by $120° \pm 10°$ or $240° \pm 10°$ throughout the whole operational band. Comparison to other FPRs in literature indicated the improved bandwidth of the proposed design. Finally, a microwave brain imaging system and the integration of the proposed FPR in its architecture have been proposed. The method to acquire data and construct image from the detected powers are also discussed in a brief way.

ACKNOWLEDGMENT

The authors would like to acknowledge the contribution of the Advanced Communication Engineering Centre (ACE), Universiti Malaysia Perlis for the support and suitable environment. Morever the discussions and supports of Dr. Rizwan Khan Jadoon and Dr. Hidayath Mirza are also acknowledged.

REFERENCES

[1] B. J. Mohammed, A. M. Abbosh, D. Ireland, and M. E. Bialkowski, "Compact wideband antenna immerssed in optimum coupling liquid for microwave imaging of brain stroke," *Prog. Electromagn. Res. C*, vol. 27, pp. 27–39, Jan. 2012.

[2] A. T. Mobashsher, "Wideband microwave imaging system for brain injury diagnosis," Ph.D. dissertation, School Inf. Technol. Elect. Eng., Brisbane, QLD, Australia, 2016.

[3] A. T. Mobashsher, P. T. Nguyen, and A. Abbosh, "Detection and localization of brain strokes in realistic 3-D human head phantom," in *IEEE MTT-S Int. Microw. Symp. Dig.*, Dec. 2013, pp. 1–3.

[4] A. T. Mobashsher and A. M. Abbosh, "Performance of directional and omnidirectional antennas in wideband head imaging," *IEEE Antennas Wireless Propag. Lett.*, vol. 15, pp. 1618–1621, 2016.

[5] L. Guo and A. M. Abbosh, "Compressive sensing for stroke detection in microwave-based head imaging," in *Proc. IEEE Antennas Propag. Soc. Int. Symp.*, Jul. 2014, pp. 1911–1912.

[6] E. C. Fear, J. Bourqui, C. Curtis, D. Mew, B. Docktor, and C. Romano, "Microwave breast imaging with a monostatic radar-based system: A study of application to patients," *IEEE Trans. Microw. Theory Techn.*, vol. 61, no. 5, pp. 2119–2128, May 2013.

[7] K. Staszek, S. Gruszczynski, and K. Wincza, "Design and accuracy analysis of a broadband six-port reflectometer utilizing coupled-line directional couplers," *Microw. Opt. Technol. Lett.*, vol. 55, no. 7, pp. 1485–1490, 2013.

[8] D. Ghosh and G. Kumar, "Six-port reflectometer using edge-coupled microstrip couplers," *IEEE Microw. Wireless Compon. Lett.*, vol. 27, no. 3, pp. 245–247, Mar. 2017.

[9] K. Staszek, S. Gruszczynski, and K. Wincza, "Six-port reflectometer providing enhanced power distribution," *IEEE Trans. Microw. Theory Techn.*, vol. 64, no. 3, pp. 939–951, Mar. 2016.

[10] N. A. M. Shukor, N. Seman, and D. N. A. Zaidel, "Wideband six-port reflectometer design formed by enhanced branch-line couplers," in *Proc. IEEE Asia–Pacific Conf. Appl. Electromagn. (APACE)*, Dec. 2014, pp. 63–66.

[11] S. P. Yeo, B. Tan, and E. H. Kwek, "Improved design for symmetrical six-port microstrip coupler (based on double-ring-with-star topology)," *IEEE Trans. Microw. Theory Techn.*, vol. 48, no. 6, pp. 1074–1077, Jun. 2000.

[12] G. Lipworth *et al.*, "Metamaterial apertures for coherent computational imaging on the physical layer," *J. Opt. Soc. Amer. A, Opt. Image Sci.*, vol. 30, no. 8, pp. 1603–1612, 2013.

[13] C. Y. Lee, K. Y. You, Z. Abbas, K. Y. Lee, Y. S. Lee, and E. M. Cheng, "S-band five-port ring reflectometer-probe system for *in vitro* breast tumor detection," *Int. J. RF Microw. Comput. Eng.*, vol. 28, no. 3, Mar. 2018, Art. no. e21198.

[14] C. Y. Lee *et al.*, "Enhanced five-port ring circuit reflectometer for synthetic breast tissue dielectric determination," *Prog. Electromagn. Res. C*, vol. 69, pp. 83–95, 2016.

[15] S. K. Judah and M. D. Judd, "Direct synthesis of the matched symmetric five-port junction from its scattering matrix," *IEE Proc. H-Microw., Antennas Propag.*, vol. 133, no. 2, pp. 95–98, Apr. 1986.

[16] S. P. Yeo and F. C. Choong, "Matched symmetrical five-port microstrip coupler," *IEEE Trans. Microw. Theory Techn.*, vol. 49, no. 8, pp. 1498–1500, Aug. 2001.

[17] D. I. Kim, K. Araki, and Y. Naito, "Properties of the symmetrical circuit and its broad-band five-port design," *IEEE Trans. Microw. Theory Techn.*, vol. 32, no. 1, pp. 51–57, Jan. 1984.

[18] A. T. Mobashsher, A. M. Abbosh, and Y. Wang, "Microwave system to detect traumatic brain injuries using compact unidirectional antenna and wideband transceiver with verification on realistic head phantom," *IEEE Trans. Microw. Theory Techn.*, vol. 62, no. 9, pp. 1826–1836, Sep. 2014.

[19] A. M. Abbosh, A. Zamani, and A. T. Mobashsher, "Real-time frequency-based multistatic microwave imaging for medical applications (Invited)," in *IEEE MTT-S Int. Microw. Symp. Dig.*, Sep. 2015, pp. 127–128.

[20] B. J. Mohammed, A. M. Abbosh, S. Mustafa, and D. Ireland, "Microwave system for head imaging," *IEEE Trans. Instrum. Meas.*, vol. 63, no. 1, pp. 117–123, Jan. 2014.

[21] M. Bialkowski, N. Seman, A. Abbosh, and W. C. Khor, "Compact reflectometers for a wideband microwave breast cancer detection system," *Afr. J. Inf. Commun. Technol.*, vol. 2, no. 3, pp. 119–125, 2006.

[22] M. E. Bialkowski, A. M. Abbosh, and N. Seman, "Compact microwave six-port vector voltmeters for ultra-wideband applications," *IEEE Trans. Microw. Theory Techn.*, vol. 55, no. 10, pp. 2216–2223, Oct. 2007.

[23] E. R. B. Hansson and G. P. Riblet, "An ideal six-port network consisting of a matched reciprocal lossless five-port and a perfect directional coupler," *IEEE Trans. Microw. Theory Techn.*, vol. 31, no. 3, pp. 284–288, Mar. 1983.

[24] K. Staszek, S. Gruszczynski, and K. Wincza, "Broadband measurements of S-parameters with the use of a single 8×8 butler matrix," *IEEE Trans. Microw. Theory Techn.*, vol. 62, no. 2, pp. 352–360, Feb. 2014.

[25] H. Arab, C. Akyel, and S. O. Tatu, "An alternative vector network analyzer incorporating a dual-band six-port junction," *Microw. Opt. Technol. Lett.*, vol. 58, no. 8, pp. 1964–1968, Aug. 2016.

[26] Y. Chen, J. J. Yao, and S. P. Yeo, "Improving design of symmetrical six-port microstrip coupler," in *Proc. Prog. Electromagn. Res. Symp.*, vol. 1, Aug. 2005, pp. 598–601.

[27] K. Haddadi and T. Lasri, "Formulation for complete and accurate calibration of six-port reflectometer," *IEEE Trans. Microw. Theory Techn.*, vol. 60, no. 3, pp. 574–581, Mar. 2012.

[28] G. F. Engen, "A (historical) review of the six-port measurement technique," *IEEE Trans. Microw. Theory Techn.*, vol. 45, no. 12, pp. 2414–2417, Dec. 1997.

[29] L. K. Yee, Z. Abbas, M. A. Jusoh, Y. K. Yeow, and C. E. Meng, "Determination of moisture content in oil palm fruits using a five-port reflectometer," *Sensors*, vol. 11, no. 12, pp. 4073–4085, Apr. 2011.

[30] S. A. Baharuddin *et al.*, "Development of five port reflectometer for reflection based sensing system," *AIP Conf. Proc.*, vol. 1808, no. 1, 2017, Art. no. 20011.

[31] G. P. Riblet and E. R. B. Hansson, "The use of a matched symmetrical five-port junction to make six-port measurements," in *IEEE MTT-S Int. Microw. Symp. Dig.*, vol. 151, no. 5, Jun. 1981, pp. 151–153.

[32] S. P. Yeo, B. Tan, and E. H. Kwek, "Rogress in electromagnetics," *IEEE Trans. Microw. Theory Techn.*, vol. 48, no. 6, pp. 1071–1074, Jun. 2000.

[33] *Summary of Optimizers*. Accessed: Jan. 21, 2018. [Online]. Available: http://edadocs.software.keysight.com/display/ads201101/Summary+of+Optimizers

[34] L. Zhao, F. Liu, X. Shen, G. Jing, Y.-M. Cai, and Y. Li, "A high-pass antenna interference cancellation chip for mutual coupling reduction of antennas in contiguous frequency bands," *IEEE Access*, vol. 6, pp. 38097–38105, 2018.
[35] A. T. Mobashsher, A. M. Abbosh, and Y. Wang, "Microwave system to detect traumatic brain injuries using compact unidirectional antenna and wideband transceiver with verification on realistic head phantom," *IEEE Trans. Microw. Theory Techn.*, vol. 62, no. 9, pp. 1826–1836, Sep. 2014.
[36] A. T. Mobashsher, K. S. Bialkowski, A. M. Abbosh, and S. Crozier, "Design and experimental evaluation of a non-invasive microwave head imaging system for intracranial haemorrhage detection," *PLoS ONE*, vol. 11, no. 4, pp. 1–29, 2016.
[37] D. Ireland and M. E. Bialkowski, "Microwave head imaging for stroke detection," *Prog. Electromagn. Res.*, vol. 21, pp. 163–175, 2011.
[38] L. Guo and A. M. Abbosh, "Optimization-based confocal microwave imaging in medical applications," *IEEE Trans. Antennas Propag.*, vol. 63, no. 8, pp. 3531–3539, Aug. 2015.
[39] E. C. Fear, X. Li, S. C. Hagness, and M. A. Stuchly, "Confocal microwave imaging for breast cancer detection: Localization of tumors in three dimensions," *IEEE Trans. Biomed. Eng.*, vol. 49, no. 8, pp. 812–822, Aug. 2002.

TOUFIQ MD HOSSAIN was born in Al-Kharj, Saudi Arabia, in 1991. He received the B.Sc. degree in electrical and electronic engineering from the Khulna University of Engineering & Technology, Khulna, in 2014, and the M.Sc. degree in communication engineering from Universiti Malaysia Perlis, in 2018. He is currently pursuing the Ph.D. degree with the Faculty of Mechanical Engineering, Universiti Malaysia Pahang. He was a Research Assistant with the Advanced Communication Engineering Centre, Universiti Malaysia Perlis, from 2016 to 2018. He has authored or co-authored five referred journals and seven international conferences. His research interests include metamaterials, flexible linear to circular polarizers for CubeSat applications, and five-port reflectometers and microwave imaging of brain injury diagnosis applications.

MOHD FAIZAL JAMLOS received the M.Sc. degree from The University of Adelaide, Australia, in 2008, and the Ph.D. degree from Universiti Teknologi Malaysia, Malaysia, in 2010. He is currently a Professor with the Faculty of Mechanical Engineering, Universiti Malaysia Pahang. He has authored or co-authored some 220 scientific publications in peer-reviewed journals and conferences. His research interests include wireless embedded systems, remote sensing, on-platform antennas, and microwave circuitry. He is a practice Professional Engineer of the Board of Engineers Malaysia, a National Medical Researcher, and a Corporate Member of the Institute Engineers Malaysia.

MOHD AMINUDIN JAMLOS was born in Malaysia, in 1986. He received the Ph.D. degree in communication engineering from Universiti Malaysia Perlis, in 2016, where he is currently a Senior Lecturer of engineering technology with the Faculty of Engineering Technology. From 2011 to 2018, he and other researchers have produced 21 journals and 25 conference papers. He holds one copyright and one pending patent for research product Alzheimer Early Detection. He is interested in doing research in microwave imaging, disease and cancer identification, dielectric material characterization, electromagnetic waves, and antennas and microwave measurements. He received nine awards in: nine Gold and one special award (SIIF 2011) in national and international exhibitions. He is professionally certified with the Mikrotik Certified Network Association and a Mikrotik Certified Routing Engineer in international recognized engineering networks.

PING JACK SOH (S'10–M'14–SM'15) was born in Malaysia. He received the B.Eng. and M.Eng. degrees in electrical engineering (telecommunication) from Universiti Teknologi Malaysia, in 2002 and 2006, respectively, and the Ph.D. degree in electrical engineering from KU Leuven, Belgium, in 2013. He is currently an Associate Professor with the School of Computer and Communication Engineering, Universiti Malaysia Perlis, and also a Research Affiliate with KU Leuven, Belgium. He is a member of the IET, ACES, and URSI, and a Graduate Member of the Board of Engineers Malaysia, the Institution of Engineers Malaysia, and the Malaysia Board of Technologist. He was a recipient of the IEEE Antennas and Propagation Society Doctoral Research Award, in 2012, the IEEE Microwave Theory and Techniques Society Graduate Fellowship for Medical Applications, in 2013, and the International Union of Radio Science (URSI) Young Scientist Award, in 2015. He is a Chartered Engineer registered with the U.K. Engineering Council.

SITI ZURAIDAH IBRAHIM was born in Limbang, Malaysia, in 1981. She received the B.E. degree in telecommunication from the University of Malaya, Malaysia, in 2004, the M.E. degree from the University Technology of Malaysia, in 2008, and the Ph.D. degree from The University of Queensland, Australia, in 2012. She is currently a Senior Lecturer with the School of Computer and Communication Engineering, Universiti Malaysia Perlis, Malaysia. Her research interest includes microwave components and its application.

MUAMMAR MOHAMAD ISA received the B.Eng. degree (Hons.) in electrical and electronics engineering from Universiti Tenaga Nasional, Malaysia, in 2003, the M.Sc. degree in microelectronic engineering from the National University of Malaysia, in 2005, and the Ph.D. degree in electric and electronic engineering from The University of Manchester, in 2012. He joined SilTerra Malaysia Sdn. Bhd as a Process Engineer. Since 2006, he has been a Lecturer with the School of Microelectronic Engineering, Universiti Malaysia Perlis, where he was promoted to a Senior Lecturer, in 2010. His research in the development of high-speed low-noise device using III–V materials for large-scale satellite communication has been recognized by the Malaysian National Space Agency for the best dissertation, in 2013. He is actively involved in microelectronics fabrication and characterization for high-speed, high-frequency, and low-noise using both silicon and III–V technologies. His current research interests include the development of μ-scale antenna targeted for agricultural and medical applications. He is a member of the Institution of Engineering and Technology and the Board of Engineers Malaysia. He is also a Professional Technologist under the Malaysia Board of Technologists.

DOMINIQUE M. M.-P. SCHREURS (S'90–M'97–SM'02–F'12) received the M.Sc. degree in electronic engineering and the Ph.D. degree from the University of Leuven, Leuven, Belgium, where she is currently a Full Professor. She is a Visiting Scientist with Agilent Technologies, Eidgenössische Technische Hochschule Zürich, and the National Institute of Standards and Technology. Her main research interests include the (non)linear characterization and modeling of active microwave devices, and (non)linear circuit design for wireless power transfer and biomedical applications. She serves for the IEEE Microwave Theory and Techniques Society (IEEE MTT-S) Administrative Committee. She is an IEEE MTT-S Distinguished Microwave Lecturer. She is the Editor-in-Chief of the IEEE TRANSACTIONS ON MICROWAVE THEORY AND TECHNIQUES. She was the Chair of the IEEE MTT-S Educational Committee and the IEEE MTT-S Technical Committee on Microwave Measurements. She also serves as an Officer for the Executive Committee of the ARFTG Organization. She was the General Chair of the 2007 and 2012 Spring ARFTG Conference. She was also a Co-Chair of the European Microwave Conference, in 2008.

ADAM NARBUDOWICZ (S'12–M'14) received the M.Sc. degree from the Gdansk University of Technology, Gdansk, Poland, in 2008, and the Ph.D. degree from the Dublin Institute of Technology, Dublin, Ireland, in 2013. From 2014 to 2016, he was a Postdoctoral Research Fellow with the Institute of High Frequency Technology, RWTH Aachen University, Aachen, Germany. He is currently an EDGE Research Fellow with the CONNECT Research Centre, Dublin Institute of Technology, focuses primarily on wireless physical-layer security for the Internet of Things. He has authored or co-authored some 50 scientific publications in peer-reviewed journals and conferences. His research interests include wireless physical-layer security, remote sensing, electrically small antennas, and microwave circuitry for full-duplex radios. He was a recipient of the 2012 DIT Inventor Competition Award for the Best Postgraduate and Staff Invention and the Best Paper Award (Third Prize) at the 2017 International Symposium on Antennas and Propagation.

MOHD FAIRUSHAM GHAZALI received the bachelor's degree, in 2002, and the Ph.D. degree in mechanical engineering from The University of Sheffield, U.K., in 2012. He was a Project Engineer with Gas Malaysia Pvt. Ltd., for two years. He joined Universiti Malaysia Pahang, as a Lecturer, where he is currently an Associate Professor with the Faculty of Mechanical Engineering and the Director of the Centre of Excellence for Advanced Research in Fluid Flow. He has shown vast interest in vibration control and thermofluid research area. He is actively involved in vibration control, automatic control engineering, modal analysis, advanced signal processing, and computational fluid dynamics research activities. He is also registered as a Corporate Member of IEM.